

Projective Transformation Rectification for Camera-captured Chest X-ray Photograph Interpretation with Synthetic Data

Authors

Chak Fong Chong

Faculty of Applied Sciences, Macao Polytechnic University, Macao SAR, China
p1604994@ipm.edu.mo

Yapeng Wang

Faculty of Applied Sciences, Macao Polytechnic University, Macao SAR, China
yapengwang@ipm.edu.mo

Benjamin Ng

Faculty of Applied Sciences, Macao Polytechnic University, Macao SAR, China
bng@ipm.edu.mo

Xu Yang*

Faculty of Applied Sciences, Macao Polytechnic University, Macao SAR, China
xuyang@ipm.edu.mo

* Corresponding author

Abstract

Automatic interpretation on smartphone-captured chest X-ray (CXR) photographs is challenging due to the geometric distortion (projective transformation) caused by the non-ideal camera position. In this paper, we proposed an innovative deep learning-based **Projective Transformation Rectification Network (PTRN)** to automatically rectify such distortions by predicting the projective transformation matrix. PTRN is trained on synthetic data to avoid the expensive collection of natural data. Therefore, we proposed an innovative synthetic data framework that accounts for the visual attributes of natural photographs including screen, background, illuminations, and visual artifacts, and generate synthetic CXR photographs and projective transformation matrices as the ground-truth labels for training PTRN. Finally, smartphone-captured CXR photographs are automatically rectified by trained PTRN and interpreted by a classifier trained on high-quality digital CXRs to produce final interpretation results. In the CheXphoto CXR photograph interpretation competition released by the Stanford

University Machine Learning Group, our approach achieves a huge performance improvement and won **first place** (**ours 0.850**, second-best 0.762, in AUC). A deeper analysis demonstrates that the use of PTRN successfully achieves the performance on CXR photographs to the same level as on digital CXRs, indicating PTRN can eliminate all negative impacts of projective transformation to the interpretation performance. Additionally, there are many real-world scenarios where distorted photographs have to be used for image classification, our PTRN can be used to solve those similar problems due to its generality design.

Keywords

Chest X-ray; Image rectification; Geometric distortion; Projective Transformation; Deep learning; Medical image analysis.

Acknowledgement

This work is funded by Macao Polytechnic University under grant number RP/ESCA-01/2021.

1. Introduction

Chest X-ray (CXR) is one of the most ubiquitous medical imaging techniques for chest disease diagnosis. CXR interpretation requires certified radiologists. However, due to the lack of resources, recently some CXRs cannot be formally reviewed by radiologists in hospitals [1]. For instance, over 300 thousand patients in England wait more than 30 days for the reports of their X-rays [2].

Recently, researchers have successfully developed various deep convolutional neural networks (CNNs) to perform automatic interpretation on digital CXRs [3][4][5], which can outperform the average level of radiologists in certain disease detection [3]. For example, in 2021, Yuan et al. [5] trained a deep learning ensemble that can automatically interpret digital CXRs into 5 pathologies with a mean AUC of 0.93 and has beaten 2.8/3 radiologists on the CheXpert dataset [6].

Unfortunately, in many developing countries and regions, traditional X-ray films are still widely used [7][8][9]. The CXR films are hard copies that cannot be directly interpreted by computer-based AI models. A quick and convenient solution to perform automatic interpretation is using a smartphone camera to take a photograph of a CXR film (referred to as *CXR film photograph*) or a digital CXR on a monitor screen (referred to as *CXR monitor*

photograph). Benefitting from the low prices and popularity of smartphones, CXR photograph interpretation can be a cheap and effective solution for countries and regions which have very limited medical resources. Moreover, the use of smartphones can facilitate both real-time and store-and-forward medical consultation to provide remote medical care and remote diagnosis [10][11]. Especially, the sudden outbreak of COVID-19 in 2020 has promoted the practical applications of telemedicine and zero-contact diagnosis. Furthermore, it can help patients who have privacy concerns that not willing to go to hospitals for radiology reports.

However, automatic interpretation on smartphone-captured CXR photographs is a very challenging task due to the visual attributes such as: (1) the CXRs in photographs could be geometrically distorted due to non-ideal camera position [12], as shown in Figure 1. The distortion is known as *projective transformation*, as the CXRs appear on flats like monitor screens or X-ray viewers. The distortions are widely varying due to different camera positions; (2) the illuminations are also varied (daylight, indoor lighting, the backlight of the monitor, etc.); (3) other visual artifacts and noises, such as camera out-focus, image noise, and moiré pattern, could appear. Therefore, the performance of current existing interpretation algorithms with well-trained CNN models on these remake CXR photographs experiences a significant decline, as those algorithms were trained on high-resolution digital CXRs [13][14][15].

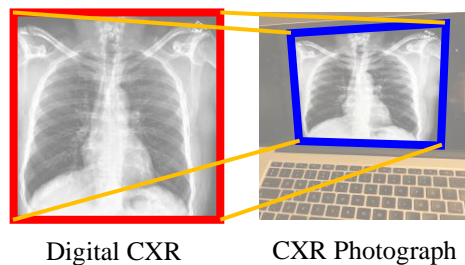


Figure 1: The CXR in a photograph experiences geometric distortion (projective transformation) due to non-ideal camera position.

Among these visual attributes, Chong et al. [14] have experimentally verified that one major reason for such performance decline is the geometric distortion (projective transformation) of CXR photographs. Several studies also have experimentally demonstrated that the geometric distortion causes significant performance declines on several image recognition tasks such as image classification [16] and text recognition [17]. Therefore, one obvious solution is to rectify the projective transformation of CXR photographs.

In the literature, deep learning-based methods have been proposed to automatically rectify the geometric distortion for different camera-captured photographs.

GAN-STAM was proposed by Chong et al. [14] that utilizes GAN [18] for rectifying the distortion of CXR photographs. However, GAN-STAM only achieves AUC 0.8653, which is still far away from the results of perfectly rectified CXR photograph (AUC 0.8867), due to (1) the lack of labeled and distorted CXR photographs for training; (2) GAN-STAM [14] uses constrained affine transformation which cannot precisely rectify projective transformation; (3) instability of GAN training; and (4) there is no quantitative metrics to evaluate the rectification accuracy.

Other deep learning-based rectification methods also have been proposed for document photograph dewarping [19][20][21] and Automatic License Plate Recognition (ALPR) [22][23] etc., which are incompatible to rectify the projective transformation on CXR photographs. Because normally a particular rectification method is only designed to solve a specific task due to various types of geometric distortion, different types of images, and available training datasets. For example, the methods for documents [19][20][21] are particularly designed for curved and folded documents, while the methods for ALPR [22][23] are for plate number recognition only, not particularly used for rectification.

In this paper, we proposed an innovative method for CXR photographs rectification, called Projective Transformation Rectification Network (PTRN). PTRN predicts the projective transformation matrices, which has not been seen in other researchers' work, to automatically rectify the projective transformation of CXR photographs precisely. Additionally, to tackle the problem of the lack of training data identified in the paper [14], we proposed an innovative framework to generate synthetic CXR photographs and projective transformation matrices as the ground truth labels for training PTRN.

The primary contributions of this work are summarized:

1. To the best of our knowledge, our innovative PTRN is the first rectification method that predicts the projective transformation matrix to rectify the projective transformation caused by non-ideal camera positions. PTRN has a simple architecture trained on synthetic data. Additionally, the Intersection over Union (IoU), which is essentially used to quantify the percent overlap for image segmentation but never be used for the evaluation of rectification performance, is firstly proposed to quantitatively evaluate the rectification performance on CXR photographs.
2. We also proposed the first synthetic CXR photograph generation framework for training, which is designed under the consideration of various interferences

encountered by photographs including screen, unwanted background, illuminations, and visual artifacts, to avoid the collection and annotation of expensive natural data. The framework produces projective transformation matrices as ground truth labels, instead of bounding boxes which are common in synthetic data generation frameworks for object detection. The speed of synthetic data generation is fast (102.89 samples/sec, i9-10900K CPU) as it only employs simple image processing methods.

3. Therefore, the automatic interpretation pipeline for CXR photographs consists of three steps: (1) PTRN predicts the projective transformation matrix of a CXR photograph; (2) The photograph is rectified using the predicted projective transformation matrix; (3) A classifier trained on high-quality digital CXRs interprets the rectified CXR photograph.

The pipeline achieves **first place** in the CheXphoto competition, which is a CXR film photograph interpretation competition hosted by Stanford and Vinbrain [24][25]. Our approach achieves AUC 0.850 which is much better than the second-best approach proposed by another researcher on the competition leaderboard (AUC 0.762).

The experiment results shown in Section 4.5 demonstrated that the pipeline successfully achieves the same AUC scores of 0.893 on both CXR photographs and digital CXRs from the same patients. This is the first work that successfully achieves the performance on CXR photographs to the same level as on digital CXRs, to the best of our knowledge. This result also demonstrates that the proposed pipeline can eliminate all negative impacts of projective transformation to the interpretation performance through rectification.

Additionally, PTRN and the synthetic data generation do not involve any semantic information and the features of the distorted image (i.e., PTRN does not need to know the distorted images are CXRs). The advantage of such an approach is the generality that can be applied to rectifying other types of distorted photographs.

The rest of the paper is organized as follows. In Section 2, work related to CXR photograph interpretation, image rectification, and deep learning with synthetic data is introduced. Section 3 introduces PTRN and the synthetic data framework. Section 4 shows the experiment results and discussion. Section 5 is the conclusion, limitations, and future work.

2. Related Work

This section summarizes the related work on CXR photograph interpretation, image rectification, and deep learning with synthetic data.

2.1. CXR Photograph Interpretation

The interpretation performance of various well-trained CNN models experiences a significant decline on CXR photographs [13][14][15].

In 2020, Le et al. [26] proposed a method to crop the CXR region in each CXR photograph using YOLO-v3 [27] to remove the unwanted background. However, the classification performance is extremely low and unacceptable (AUC 0.684).

In 2021, Kuo et al. [13] developed a recalibration method, which used data augmentation methods to add additional noises into original digital CXR images for training classifiers. Their method achieves mean AUC 0.835 on CXR photographs. However, their work focused on visual artifacts and noises. The negative impact of geometric distortion has not been tackled.

In 2021, Chong et al. [14] experimentally verified that perfectly rectifying the geometric distortion of CXR photographs can improve classification performance from AUC 0.8009 to AUC 0.8867, which is very close to the performance on digital CXRs (AUC 0.8888, only AUC 0.0021 is dropped). They also proposed GAN-STAM to automatically rectify the geometric distortion of CXR photographs. However, the classifiers achieved only AUC 0.8653 on automatically rectified CXR photographs. GAN-STAM cannot eliminate all the negative impacts of geometric distortion, as GAN-STAM has several limitations: (1) GAN-STAM uses constrained affine transformation to rectify CXR photographs. However affine transformation cannot precisely rectify the distortion, as the distortion is projective transformation [28]. (2) the lack of data. Only around 10k CXR photographs are available for training, leading to a bad rectification performance; (3) the training of GAN is instable [29][30]; and (4) there is no quantitative evaluation metric to measure the rectification performance.

2.2. Geometric Distortion Rectification for Camera-captured Photographs

Traditional non-AI based methods to solve the geometric distortion rectification problem for camera-captured photographs have been proposed for document photographs [31][32][33], QR code photographs [34][35], etc. For a document photograph, horizontal sentences printed in the document are utilized by using image processing techniques like Radon transformation [36][33] to calculate the distortion of the document such as the vanishing points and the level of curving. For a QR code photograph, the features (finder patterns and alignment patterns) which only shown in QR codes are utilized to locate the QR codes for rectification. Overall, a particular method is designed only for solving a specific task as the features of different types of images vary.

Deep learning has been utilized for such rectification tasks. In comparison to traditional methods, deep learning-based methods can learn from a large amount of data like photographs captured in different scenarios. Therefore, it is more robust to perturbed images like camera-captured natural photographs. It also reduces the manual design of algorithms.

However, to the best of our knowledge, current rectification methods are incompatible with photographs like CXR photographs which experience projective transformation.

A task that benefits from deep learning is document dewarping. A document in a camera-captured photograph is curved and folded. Traditional methods are difficult to model such complicated distortions, whereas deep learning algorithms can achieve good performance by learning from a large amount of data. DocUNet [19] rectifies curved and folded documents by directly predicting the pixels' mappings from the source distorted image to the ground truth flat image. DewarpNet [20] achieves rectification in the way similar to DocUNet but further exploits 3D shape representation to improve the rectification performance. These methods are trained on synthetic data like Doc3D [20]. However, these methods are particularly designed for curved and folded documents, which are incompatible with photographs that experienced projective transformation.

Another example is Automatic License Plate Recognition (ALPR) which requires deep learning-based methods, as the appearances of plate photographs captured by CCTV cameras vary, including different illuminations, weather, etc. Silva and Jung [23] proposed an object detection network called IWPOD-NET which predicts both the object probability and the 6-parameters of the affine transformation to locate a distorted object. Björklund et al. [22] proposed an object detection network trained with synthetic data to predict both the object probability and the corners of the plate. However, these networks cannot perform precise geometric distortion rectification on camera-captured photographs like CXR photographs, since (1) the purposes of these networks are image recognition, instead of image rectification; and (2) they used affine transformation to reduce the distortion, which cannot precisely rectify the distortion (projective transformation) caused by non-ideal camera position in theory [28]. Therefore, these methods are incompatible with photographs that experienced projective transformation.

Besides, deep learning algorithms are also proposed for rectifying other camera-captured photographs such as barcodes [37] and text [17]. The method for barcodes involves the appearances of barcodes (vertical lines), while the geometric distortions of texts include text

line curvature which is very different from CXR photographs. Therefore, these rectification methods are also incompatible with photographs that experience projective transformation.

Therefore, we proposed an innovative PTRN which is the first method that predicts the projective transformation matrix of a photograph to rectify the projective transformation caused by non-ideal camera position.

2.3. Synthetic Data on Camera-captured Photograph Geometric Distortion Rectification and Object Detection

Synthetic data is one popular method to solve the problem of the lack of data for training deep learning models, as it avoids collecting expensive natural data and annotations. Synthetic data has also been used for object detection [38][39][40] and camera-captured photograph geometric distortion rectification tasks [19][20][22].

The common strategy for generating a synthetic image is a composition of a foreground image (i.e., a geometrically distorted object) and a background image, plus data augmentation to simulate the perturbations of camera-captured photographs [19][20][22][38][39][40]. However, the generation steps for different types of images are quite different as the visual attributes across different images are various. For example, in text detection [38], a text usually appears in well-defined regions like a sign or a flat wall. Therefore, the generation step includes geometric estimation and segmentation to ensure the texts are properly placed in the correct positions.

Moreover, the ground truth labels of synthetic data for different tasks are very different. For object detection, bounding boxes are used to locate the objects. For image dewarping, the ground truth labels are grid meshes.

Our proposed framework for synthetic data generation has a couple of novelty in comparison to previous synthetic data frameworks. We proposed the first framework for CXR photograph generation. The design of the framework is under consideration of the visual attributes of CXR photographs. Furthermore, our framework is the first that uses the projective transformation matrix as the ground truth to represent the distortion caused by the non-ideal camera position. Unlike object detection tasks that use bounding boxes that only locate the object, the projective transformation parameters can be used to locate and rectify the image, as the recognition performance could achieve higher after rectification [14][17]. Which is innovative and effective.

3. Methods

To tackle the identified limitations of GAN-STAM [14] which is a previous work of CXR photograph rectification, we have proposed PTRN: (1) PTRN aims to rectify the projective transformation of distorted CXR photographs by predicting the projective transformation matrices. (2) We generate synthetic CXR photographs to solve the problem of the lack of training data; (3) PTRN is trained in an end-to-end manner, which avoids the instability of GAN training; and (4) We proposed a quantitative evaluation method (IoU) to measure the rectification performance for such rectification algorithms. Therefore, PTRN achieves a huge improvement in comparison to GAN-STAM. The experiment in Section 4.5 demonstrates PTRN can eliminate all negative impacts of geometric distortion of CXR photographs to the interpretation performance.

3.1. Problem Formulation

This section formulates the problem of geometric distortion rectification for CXR photographs. The designs of PTRN and the synthetic data framework are based on the following formulations.

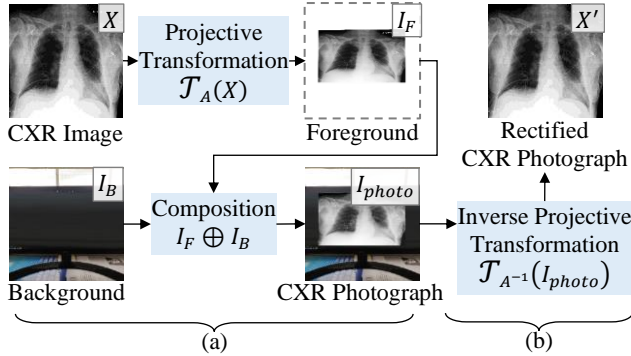


Figure 2: Formulation of geometric distortion rectification for CXR photographs.

A CXR photograph I_{photo} can be treated as a composition of a distorted CXR image I_F and a background image I_B (Figure 2(a)). We borrow a notation \oplus from [41] to represent the composition of two images. I_{photo} can be formulated as:

$$\begin{aligned} I_{photo} &= I_F \oplus I_B \\ &= \mathcal{T}_A(X) \oplus I_B \end{aligned} \quad (1)$$

where I_F is a CXR image X warped by projective transformation with a 3-by-3 transform matrix A : $I_F = \mathcal{T}_A(X)$. A matrix A has 8 parameters θ_i that represent a projective

transformation: $A = \begin{bmatrix} \theta_1 & \theta_2 & \theta_3 \\ \theta_4 & \theta_5 & \theta_6 \\ \theta_7 & \theta_8 & 1 \end{bmatrix}$. In this work, all projective transformations are applied in

the homogeneous coordinates and the coordinates of the 4 vertices of each image are assigned

to be $P_0 = \left\{ \begin{pmatrix} -1 \\ -1 \\ 1 \end{pmatrix}, \begin{pmatrix} 1 \\ -1 \\ 1 \end{pmatrix}, \begin{pmatrix} 1 \\ 1 \\ 1 \end{pmatrix}, \begin{pmatrix} -1 \\ 1 \\ 1 \end{pmatrix} \right\}$.

A CXR photograph I_{photo} can be rectified using inverse projective transformation if the matrix A is known (Figure 2 (b)):

$$X' = \mathcal{T}_{A^{-1}}(I_{photo}) \quad (2)$$

where X' denotes the rectified I_{photo} .

The design of PTRN (Section 3.2) is based on Eq. (2). A CXR photograph I_{photo} can be automatically rectified by predicting the matrix A . Therefore, a training sample (I_{photo}, A) for PTRN consists of a CXR photograph I_{photo} and the ground truth matrix A .

The design of the synthetic data framework (Section 3.3) is based on Eq. (1). A training sample (I_{photo}, A) can be synthesized using a random CXR image X , a random background I_B and a randomly generated matrix A .

3.2. Projective Transformation Rectification Network

We proposed the Projective Transformation Rectification Network (PTRN) for rectifying the projective transformation of CXR photographs. PTRN predicts the projective transformation matrix A of a CXR photograph I_{photo} . PTRN is similar to the localization net of STN [42] which both predict the transformation parameters. However, PTRN is trained directly using synthetic data while STN is trained using the gradients propagated from back layers.

3.2.1. Architecture

PTRN has a simple architecture, as shown in Figure 3 (right). It consists of two components: (1) a CNN backbone (e.g., ResNet-50 [43], DenseNet-121 [44]), followed by (2) an 8-unit FC layer that regresses the 8 parameters $\hat{\theta}_i$ of a predicted matrix \hat{A} . This simple architecture enables easy implementation on various deep learning frameworks.

Rectifying a CXR photograph using PTRN has two steps, as shown in Figure 3: (1) PTRN predicts \hat{A} ; (2) Apply the inverse projective transformation (Eq. (2)) to the CXR photograph with \hat{A} .

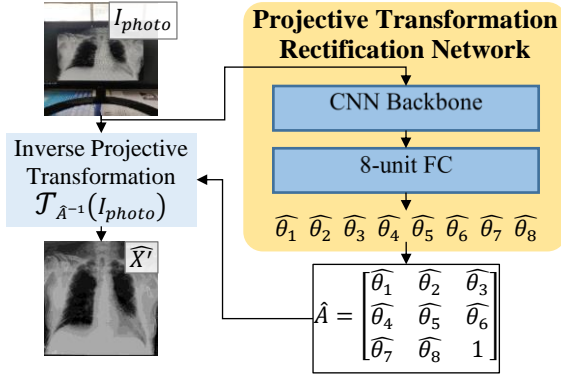


Figure 3: The architecture of Projective Transformation Rectification Network (PTRN) with the steps of rectifying a CXR photograph using PTRN.

3.2.2. CXR Region Prediction

A matrix A can be converted to a quadrilateral that represents a CXR region. The 4 vertices

$\begin{pmatrix} x_i \\ y_i \\ 1 \end{pmatrix}$ of the quadrilateral represented by A are:

$$\begin{pmatrix} w_i x_i \\ w_i y_i \\ w_i \end{pmatrix} = A \begin{pmatrix} u_i \\ v_i \\ 1 \end{pmatrix} \quad (3)$$

where $\begin{pmatrix} u_i \\ v_i \\ 1 \end{pmatrix} \in P_0 = \left\{ \begin{pmatrix} -1 \\ -1 \\ 1 \end{pmatrix}, \begin{pmatrix} 1 \\ -1 \\ 1 \end{pmatrix}, \begin{pmatrix} 1 \\ 1 \\ 1 \end{pmatrix}, \begin{pmatrix} -1 \\ 1 \\ 1 \end{pmatrix} \right\}.$

The quadrilateral can also be converted back to a matrix A using Eq. (3). This relation is used in the evaluation of the rectification performance of PTRN. For instance, a predicted matrix \hat{A} can be converted to a predicted CXR region.

3.2.3. Training

PTRN is trained with synthetic training samples $\left\{ \left(I_{photo}^{(i)}, A^{(i)} \right) \right\}$ in an end-to-end manner. As

PTRN predicts the parameters by regression, mean squared error (MSE) loss is used to calculate the loss between the model prediction and the ground truth. MSE loss is defined as

$$loss = \frac{1}{N} \sum_{i=1}^N (y_i - \hat{y}_i)^2$$

where y denotes the 8 parameters of the ground truth A : $y = [\theta_1 \ \theta_2 \ \theta_3 \ \theta_4 \ \theta_5 \ \theta_6 \ \theta_7 \ \theta_8]$ and \hat{y} denotes the predicted 8 parameters $\hat{y} = [\hat{\theta}_1 \ \hat{\theta}_2 \ \hat{\theta}_3 \ \hat{\theta}_4 \ \hat{\theta}_5 \ \hat{\theta}_6 \ \hat{\theta}_7 \ \hat{\theta}_8]$.

3.2.4. Rectification Performance Evaluation

PTRN is evaluated on validation/test samples $\{(I_{photo}^{(i)}, P^{(i)})\}$. Each sample consists of a natural CXR photograph I_{photo} and the 4 vertices $\begin{pmatrix} x_i \\ y_i \\ 1 \end{pmatrix} \in P$ of the ground-truth CXR region.

The ground-truth label is the 4 vertices instead of matrix A since marking the 4 vertices is the simplest way to annotate ground-truth labels in practice.

We proposed using IoU between the ground truth CXR region and the predicted CXR region for each sample to measure the rectification performance, as the predicted region should be as overlapped as the ground truth region. The predicted region is calculated from the predicted matrix \hat{A} using Eq. (3) and the ground truth region is given in the validation/test samples. The IoU calculation of a sample is demonstrated in Figure 4.

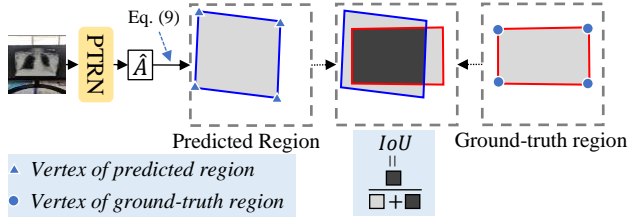


Figure 4: The rectification performance of PTRN is evaluated by the IoU between predicted regions and ground truth regions.

3.3. Training Data Synthesis

Our proposed PTRN is deep learning-based, which requires a large amount of training data. Unfortunately, there are no suitable public CXR datasets. Collection and annotation of natural data samples that include CXR photographs and ground-truth labels are also expensive. Therefore, we proposed a framework for the generation of synthetic training samples. The generation of one synthetic training sample consists of 4 steps, as shown in Figure 5: (1) screen synthesis; (2) CXR projective transformation; (3) adding a background image; and (4) adding illumination, visual artifacts and noises. A random digital CXR X and a random image R are required for generating a sample. The details of the 4 steps are described in the following subsections. Note that the design of the framework does not exactly follow Eq. (1), as various interferences are also considered including the *screen*, *background*, *illuminations*, and *artifacts*. Randomness is involved in the framework to increase the diversity of synthetic CXR photographs so that hopefully the trained PTRN can be generalized to photographs captured in various scenarios. An ablation study is conducted in Section 4.6 to verify the framework. The

framework only employs simple image processing methods such as transformation, composition, and simple augmentation methods. Through experiment, the generation speed is around 102.89 samples/second in a PC with Intel i9-10900K CPU.

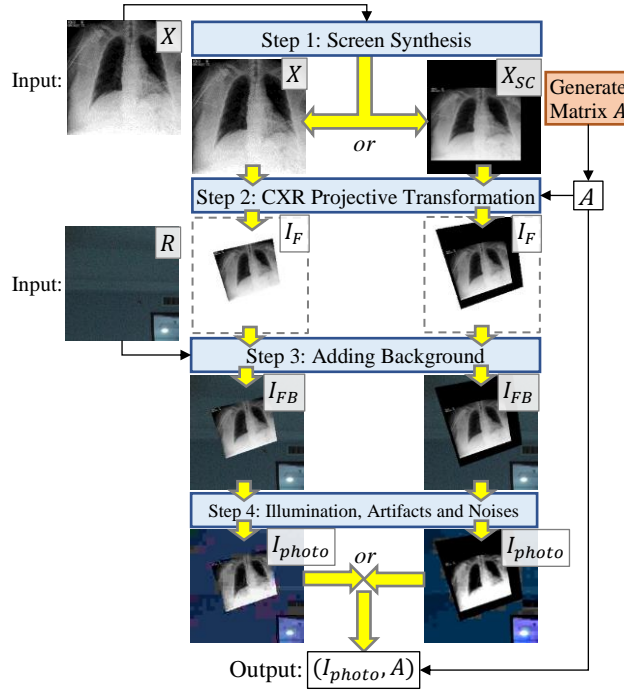


Figure 5: The steps to generate a synthetic training sample.

3.3.1. Screen Synthesis



Figure 6: The distorted CXR is surrounded with a dark area.

In a CXR photograph, the distorted CXR is normally surrounded by a dark area, which is usually a monitor screen, as shown in Figure 6. The appearances of the dark areas look like a part of the CXR. This step is to synthesize such a situation to improve the robustness of PTRN in this situation.

Considering that not all the CXR photographs have such a situation, in experiments, the probability of screen synthesis is set to be 0.3. If the screen is synthesized, the output of this step is a CXR with a synthetic screen X_{SC} , otherwise, the output is identical to the input X .

The process of screen synthesis has two steps, as shown in Figure 7.

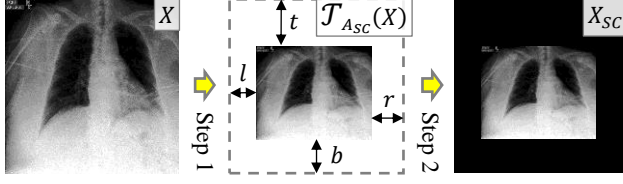


Figure 7: The two steps of screen synthesis.

Step 1: X is scaled-down and translated, determined by the randomly generated padding sizes t, b, l, r (see Figure 7). In the experiments, we set: $t, b, l, r \sim U_{[0,0.6]}$. Subsequently, the operation of scaling down and translation is implemented by projective transformation. The transform matrix A_{SC} is calculated by:

$$A_{SC} = \begin{bmatrix} 1 - (l + r)/2 & 0 & (l - r)/2 \\ 0 & 1 - (t + b)/2 & (t - b)/2 \\ 0 & 0 & 1 \end{bmatrix} \quad (4)$$

. Finally, X is scaled-down and translated: $\mathcal{T}_{A_{SC}}(X)$.

Step 2: $\mathcal{T}_{A_{SC}}(X)$ and a plain dark color image I_{color} are composited to get the output X_{SC} :

$$X_{SC} = \mathcal{T}_{A_{SC}}(X) \oplus I_{color} \quad (5)$$

. In the experiments, the RGB values of the I_{color} is randomly generated by $R, G, B \sim U\{0, 19\}$.

3.3.2. CXR Projective Transformation

This step is to simulate the projective transformation caused by the non-ideal camera position.

Firstly, a projective transformation matrix A is randomly generated to determine how a CXR is distorted geometrically (i.e., A determines the position of the distorted CXR). Then, projective transformation with matrix A is applied to the output of step 1 to get a distorted CXR I_F .

The 8 parameters θ_i of A must be generated under some regulations since an inappropriate set of parameters results in a nonsensical distorted CXR, e.g., the shape is non-convex [45][28]. Therefore, to avoid such unexpected situations, we split the matrix A into a sequential series of actions: *scaling*, *shearing*, *rotation*, *perspective warp* and *translation*. Subsequently, the parameters of these actions are generated within an appropriate range (e.g., the parameters of shearing cannot be too large).

The transformation of matrix A is split into the 5 actions:

$$A = \begin{bmatrix} \theta_1 & \theta_2 & \theta_3 \\ \theta_4 & \theta_5 & \theta_6 \\ \theta_7 & \theta_8 & 1 \end{bmatrix} = A_T A_P A_R A_S A_C \quad (6)$$

where A_T, A_P, A_R, A_S, A_C denote the transform matrix of translation, perspective warp, rotation, shearing, and scaling, respectively. The matrices are:

$$A_T = \begin{bmatrix} 1 & 0 & T_x \\ 0 & 1 & T_y \\ 0 & 0 & 1 \end{bmatrix}, A_P = \begin{bmatrix} 1 & 0 & 0 \\ 0 & 1 & 0 \\ P_x & P_y & 1 \end{bmatrix}, A_R = \begin{bmatrix} \cos \alpha & \sin \alpha & 0 \\ -\sin \alpha & \cos \alpha & 0 \\ 0 & 0 & 1 \end{bmatrix},$$

$$A_S = \begin{bmatrix} 1 & S_x & 0 \\ S_y & 1 & 0 \\ 0 & 0 & 1 \end{bmatrix}, A_C = \begin{bmatrix} C_x & 0 & 0 \\ 0 & C_y & 0 \\ 0 & 0 & 1 \end{bmatrix}$$

where $T_x, T_y, P_x, P_y, \alpha, S_x, S_y, C_x, C_y$ are the parameters of the actions, and they are randomly generated. In the experiment, we set:

Scaling parameters C_x, C_y . They are generated by: $C_x, C_y \sim U_{[0.2, 0.8]}$ for scaling down. If $|C_x - C_y|$ is too large, the transformed CXR will be too narrow. Therefore, a constraint $|C_x - C_y| \leq 0.2$ is set up.

Rotation parameter α . The orientation of the CXR in a photograph may not be correct. The radian α for rotation can be any: $\alpha \sim U_{[-\pi, \pi]}$.

Other parameters. $S_x, S_y, P_x, P_y, T_x, T_y$ should not be too large. They are generated by:

$$S_x, S_y \sim U_{[-0.1, 0.1]}$$

$$T_x, T_y \sim N(\mu = 0, \sigma^2 = 0.25^2)$$

$$F_x, F_y \sim N(\mu = 0, \sigma^2 = 0.1^2)$$

The generated matrix A is then used to transform the output of step 1 to calculate the distorted CXR I_F . Step 1 has two types of outputs: X and X_{SC} . In the case of X , I_F is calculated by

$$I_F = \mathcal{T}_A(X) \quad (7)$$

. In the case of X_{SC} , since the CXR region in X_{SC} has been transformed by A_{SC} , the transformation by A_{SC} must be inversed to ensure that A can correctly represent the CXR region in I_F . The distorted CXR I_F is calculated by

$$I_F = \mathcal{T}_{AA_{SC}^{-1}}(X_{SC}) \quad (8).$$

3.3.3. Adding Background Image

In practical situations, the background of a CXR photograph varies. We consider it as a random image R . This step is to composite the output I_F of step 2 and a background image. The output I_{FB} is calculated by

$$I_{FB} = I_F \oplus R \quad (9).$$

3.3.4. Adding Illumination, Visual Artifacts, and Noises

The goal of this step is to make the synthetic CXR photographs more challenging than the natural CXR photographs so that our rectification approach could be more generalized. In the experiments, various data augmentation methods are used to simulate the natural environment such as illumination, visual artifacts and noise, as listed in Table 1.

Simulation	Data Augmentation Methods
Illuminations	Adding pixel values
	Multiplying pixel values
	Adding hue and saturation value in HSV
	Color Enhancement
	Brightness Enhancement
	Sharpness enhancement
Out-focus	Average blur
Image noises	Adding Gaussian noise
Image compression	JPEG compression

Table 1: Methods which are used in experiments.

In the end, I_{photo} and matrix A are composited to be a synthetic training sample (I_{photo}, A) .

Figure 8 shows some samples of generated I_{photo} .



Figure 8: Some samples of synthetic CXR photographs.

4. Experimental Results and Discussion

All experiments are conducted on Python 3 with TensorFlow 2 framework. The data augmentation methods are implemented by using imgaug library.

4.1. Datasets

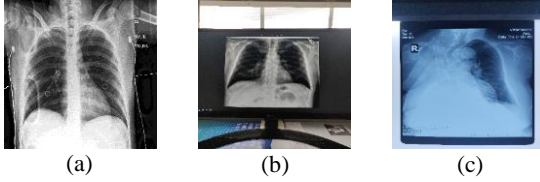


Figure 9: (a) CheXpert validation set. (b) CheXphoto-Monitor validation set. (c) CheXphoto-Film validation set.

4.1.1. CheXpert

CheXpert [6] is a public digital CXR image dataset for competition. It consists of 224,316 digital CXRs from 65,240 patients. Each digital CXR is labeled into at least one of 14 pathologies: *No Finding*, *Enlarged Cardiomediastinum*, *Cardiomegaly*, *Lung Opacity*, *Lung Lesion*, *Edema*, *Consolidation*, *Pneumonia*, *Atelectasis*, *Pneumothorax*, *Pleural Effusion*, *Pleural Other*, *Fracture*, and *Support Devices*. The validation set consists of 234 digital CXRs from 200 studies (Figure 9 (a)).

4.1.2. CheXphoto

CheXphoto [24] is a public CXR photograph dataset for competition. It consists of 10,507 smartphone-captured CXR photographs from 3,000 patients, which are generated from some digital CXR images in CheXpert. The label for each CXR photograph is inherited from CheXpert. The validation set consists of synthesis photographs and natural photographs. In the experiments conducted in this paper, only natural photographs are used for evaluation. The validation set has two types of natural photographs: (1) A total of 234 CXR monitor photographs (Figure 9(b)). They are the photograph version of the CheXpert validation set. Each photograph is produced by using a smartphone camera to capture digital CXRs displayed on a monitor. (2) A total of 250 CXR film photographs (Figure 9(c)). Each photograph is produced by photographing CXR films using a smartphone.

In Section 4.4, PTRN is used for the CheXphoto competition. In the competition, the private test CXR photographs were split into two private test sets by type (monitor/film). Therefore, we split the CheXphoto validation set into two sets by the type (monitor/film) for experiments, referred to as *the CheXphoto-Monitor validation set* and *the CheXphoto-Film validation set*,

respectively. Note that the CheXphoto-Monitor validation set is the photograph version of the CheXpert validation set (digital CXR), we used these two sets to demonstrate the effectiveness of PTRN in Section 4.5.

4.2. Implementation Details of PTRN

In the implementation, a DenseNet-201 [44] pretrained on the ImageNet dataset [46] is used as the backbone network. Adam optimizer [47] with a learning rate of 1×10^{-5} and parameters ($\beta_1 = 0.9, \beta_2 = 0.999, \epsilon = 1 \times 10^{-7}$) is used to update the weights. The batch size is set to 32. The input image is a 224×224 pixel RGB image. Pixel values are rescaled linearly from $[0, 255]$ to $[0, 1]$.

Among these hyperparameters, only the learning rate was simply tuned while others remain default. The trained PTRN has sufficient rectification performance already (see Section 4.6), which verifies the effectiveness of this approach.

PTRN is trained on synthetic data. The generation of synthetic training samples requires CXR images and random images. We used the 224,316 digital CXRs from the CheXpert training set as the source of the CXR images, and the 41K images from the Microsoft COCO 2017 test set [48] as the source of the random images. When generating a sample, a CXR image and a random image are randomly picked from the sources. Benefitting from the generation speed of synthetic data, we dynamically generate the synthetic training data during training. Therefore, each training sample is used only once to avoid overfitting.

The performance of PTRN is validated on the CheXphoto-Monitor validation set per 100 weights updates. The model with weights that achieves the highest IoU on the validation set is picked and furtherly tested on the CheXphoto-Film validation set.

The evaluation of PTRN requires the 4 vertices of the ground truth region for each validation/test sample. Since both CheXphoto-Monitor and CheXphoto-Film validation sets did not annotate the ground truth of the CXR region in each photograph, we manually annotated the 4 vertices of the distorted CXR in each photograph as the ground truth label.

4.3. CXR Interpretation Pipeline

The pipeline to perform CXR photograph interpretation, as shown in Figure 10, consists of three steps: (1) PTRN predicts the projective transformation matrix A of a CXR photograph; (2) the photograph is rectified using the predicted matrix \hat{A} ; (3) A classifier trained on high-

quality digital CXRs interprets the rectified CXR photograph. This pipeline is used in the experiments shown in Sections 4.4 and 4.5.

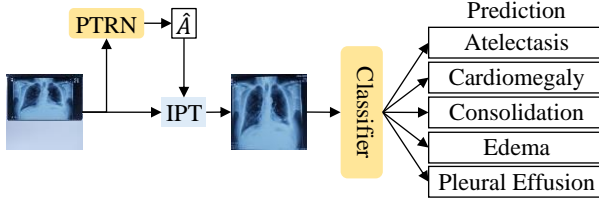


Figure 10: CXR photograph interpretation pipeline.

4.4. *CheXphoto Competition*

CheXphoto is a competition for X-ray interpretation based on smartphones captured CXR films photographs and CXR monitor photographs, hosted by Stanford and VinBrain [24]. A submitted model is tested to perform multi-label classification on the two private test sets, respectively:

1. CXR film photographs. A total of 250 CXR films are captured as photographs by a smartphone camera. The ranking of the leaderboard is sorted in terms of AUC on this private test set. We refer to this set as *CheXphoto-Film private test set*.
2. CXR monitor photographs. A total of 668 digital CXRs from 500 studies are displayed on a monitor and captured as photographs by an iPhone 8. We refer to this set as *CheXphoto-Monitor private test set*.

The performance of a model is measured by calculating the mean AUC-ROC score on 5 selected pathologies: *Atelectasis*, *Cardiomegaly*, *Consolidation*, *Edema*, and *Pleural Effusion*.

We built a CNN ensemble classifier for this competition with the pipeline in Section 5.3. The classifier consists of 5 weighted average ensembles. Each ensemble corresponds to output the predicted probability of a pathology. Each ensemble is composed of 4~6 well-trained single classifiers. A single classifier aims to perform binary classification of a pathology on the rectified CXR photographs. A single classifier is a CNN model with an input of 224×224 pixel grayscale image. Unlike other previous work, a single classifier only predicts one pathology instead of all 5 pathologies. It is due to the numbers of training samples across the 5 pathologies are quite unbalanced. While training a multi-label classifier, the times of overfitting for different labels are different. Therefore, we employed binary classifiers to obtain optimal performance for each pathology.

The single classifiers are trained on the CheXpert training set. The single classifiers are trained with different configurations to improve the performance of the constructed ensembles [49][50]. The different configurations include different CNN models, learning rates, batch sizes, configurations of label smoothing regularization from [4] for handling uncertainty labels, and data augmentation methods such as adjusting brightness, contrast, and adding Gaussian noise. Cross entropy loss is used to calculate the loss. The validation dataset is the CheXphoto-Film validation set in which the geometric distortion is perfectly rectified by manual operation.

The results in the CheXphoto competition of the pipeline are reported in Table 2. PTRN outperforms the work in [26] and [14], which are published in the literature. Since the CXRs of these validation/test sets are from different patients, the AUC scores are not comparable across different sets.

By the time of this manuscript submission, our pipeline achieves first place on the leaderboard [25], as shown in Table 3. The first, second, and third places are all our work based on PTRN. As the competition is released recently, there is no published work on the leaderboard. We compare our pipeline with the fourth place, our approach yields a huge performance gap on CXR film photographs (0.850 vs. 0.762, 0.088 higher in AUC).

Method	CXR Film Photograph		CXR Monitor Photograph	
	Validation	Test	Validation	Test
YOLOv3 [26]	-	-	0.684	-
GAN-STAM [14]	-	-	0.865	-
PTRN (Ours)	0.868	0.850	0.885	0.891

Table 2: Quantitative results in AUC of PTRN on the CheXphoto validation sets and the CheXphoto competition private test sets.

Rank	Model	CXR Film Photograph	CXR Monitor Photograph
1	LBC-v2	0.850	0.89
2	LBC-v0	0.820	0.89
3	Stellarium-CheXpert-Local	0.802	0.88
4	MVD121	0.762	0.83
5	MVD121-320	0.758	0.84

Table 3: The top 5 of the leaderboards of the CheXphoto competition (28 Apr 2022). The top 3 spots are all our PTRN.

4.5. Interpretation Performance of a Classifier on Automatically Rectified Photographs

To verify the performance improvement in the CheXphoto competition is mostly contributed by PTRN instead of the ensembling, we compare the performance of a CNN classifier with/without PTRN on CXR photographs.

The CNN classifier is an Xception [51] that was trained on the CheXpert dataset only. The CNN achieves AUC 0.889/0.887 on the CheXpert validation/test set, respectively. The performance is close to the single model of #2 [4] in the CheXpert competition (validation AUC 0.894). This CNN model has been uploaded to the CheXphoto competition. In the leaderboard, the name of the CNN without PTRN is *Stellarium*, and the name of the CNN with PTRN is *Stellarium-CheXpert-local*. The results are shown in Table 4.

Method	CheXpert		CheXphoto-Monitor		CheXphoto-Film	
	Validation	Private Test	Validation	Private Test	Validation	Private Test
CNN	0.889	0.887	0.821	0.710	0.722	0.599
PTRN + CNN	0.893+0.004	0.896+0.009	0.893+0.072	0.880+0.170	0.791+0.069	0.802+0.203

Table 4: Quantitative results in AUC of the CNN classifiers on validation sets and private test sets.

The first row reports the performance of the CNN without PTRN, huge performance drops of this CNN are observed on the CXR monitor photographs and CXR film photographs, since the photographs experienced projective transformation with extra noises such as visual artifacts.

In the second row, PTRN is used to rectify the projective transformation of CXR photographs. The interpretation pipeline follows the one in Section 4.3.

For the results on the CXR monitor photographs, this pipeline achieves AUC 0.893/0.880 on the validation/test set, respectively, which is far superior to the AUC scores before rectification (AUC 0.821/0.710). The data in the CheXphoto-Monitor validation set is the photograph version of the digital CXRs in the CheXpert validation set. The performance on the CheXphoto-Monitor validation set (AUC 0.893) is the same as the performance on the CheXpert validation set (AUC 0.893). It indicates that PTRN is sufficient to maintain the classification performance on CXR photographs to the same level as on digital CXRs. This result demonstrates that PTRN is sufficient to eliminate all the negative impacts of projective transformation to interpretation performance.

In CXR film photographs, huge performance improvements are observed after using PTRN (AUC 0.802/0.599, 0.203 improvement on the CheXphoto-Film private test set), which verifies the effectiveness of the PTRN on both types of photographs, and the performance on CXR photographs can be improved by rectification.

Besides, we furtherly test this pipeline in the CheXpert dataset. Surprisingly, minor improvements are also observed. A further investigation is needed to verify the performance impact of PTRN on digital CXRs.

4.6. Ablation Study on Training Sample Synthesis

The synthetic data framework consists of 4 steps. However, from Eq. (1), a synthetic CXR photograph can be composited by only the distorted CXR and a background. It means in the framework, only step 2 (projective transformation) and 3 (adding background) are necessary. Step 1 (screen synthesis) and step 4 (adding illumination, visual artifacts and noises) are additional to simulate the visual attributes of CXR photographs. To study the rectification performance impact of steps 1 and 4, we conducted an ablation study by removing step 1 or/and 4.

Step				CheXphoto-Monitor Validation (for validation)	CheXphoto-Film Validation (for test)
1	2	3	4		
✓	✓	✓	✓	0.942 (0.938, 0.946)	0.892 (0.887, 0.898)
	✓	✓	✓	0.911 (0.905, 0.916)	0.816 (0.808, 0.824)
✓	✓	✓		0.919 (0.914, 0.924)	0.800 (0.790, 0.809)
	✓	✓		0.881 (0.875, 0.886)	0.815 (0.807, 0.824)

Table 5: Ablation study on the framework for generation of synthetic data (In mean IoU with 95% C.I.).

The results are shown in Table 5. Mean IoU (mIoU) with 95% confidence interval (C.I.) is reported. In the first row, the mIoU of PTRN that is trained with all four steps is reported. It achieves mIoU 0.942/0.892 on the validation/test set respectively. After removing the step(s), the mIoU on the validation set are dropped by approximately 0.02-0.07, and the mIoU on the test set are dropped much larger (approximately 0.07-0.10). It demonstrates the necessity and importance of step 1 and 4. It also verifies that the framework for the generation of synthetic CXR photographs has sufficient variance of the key variables controlling the distorted CXRs.

4.7. Qualitative Evaluation of PTRN

In Figure 11, we demonstrate using trained PTRN to automatically rectify six CXR photographs captured in different scenarios. All six CXR photographs are properly. Especially in the fifth photograph from the left, even if parts of the CXR region are cropped, PTRN can still accurately predict the region and perform rectification. It is because some synthetic samples also have such situations (see Figure 8). These results demonstrate that PTRN is robust to CXR photographs captured in different scenarios.

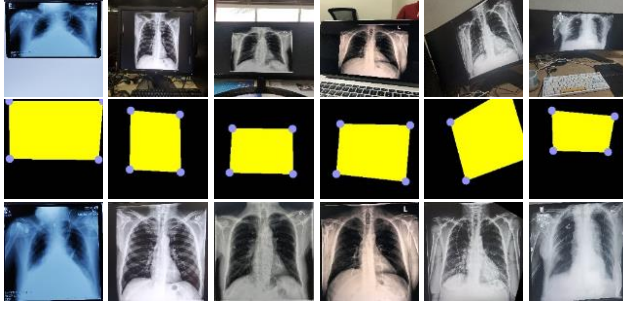


Figure 11: Top row: CXR photographs. Mid row: Prediction of PTRN. Bot row: CXR photographs that are rectified by using the prediction.

5. Conclusion

In this paper, we presented a deep learning-based Projective Transformation Rectification Network (PTRN) that is trained with synthetic data for rectifying the projective transformation of CXR photographs. We also proposed a framework to generate synthetic data. Our pipeline achieves first place on the CheXphoto competition leaderboard, which has a significant improvement over [26] and [14]. This result verifies the performance of our PTRN and the framework for the generation of synthetic data. Additionally, the design of PTRN and the framework for the generation of synthetic data can be applied to other image recognition fields that encounter similar image distortion caused by the imperfect camera position.

This work has certain limitations. In Section 4.2, the hyperparameters were not particularly tuned in the training of PTRN since it already produced satisfying rectification performance. The performance could be further improved by tuning hyperparameters or choosing other CNNs as the backbone. Moreover, further investigation is needed to verify the generalization of PTRN on CXR photographs captured in more scenarios.

We used chest X-ray photographs to demonstrate the effectiveness of our approach, which may also apply in other types of medical imaging such as CT and MRI, or other fields such as Automatic License Plate Recognition. A further investigation is needed to verify.

The above limitations may lead to possible directions to extend or improve this work. The final goal for us is developing a smartphone application for automatic medical imaging interpretation using this work to improve global public health.

References

- [1] C. Q. Commission, “Radiology review: a national review of radiology reporting within

the NHS in England,” *Care Qual. Comm.*, 2018.

- [2] Royal College of Radiologists, “Unreported X-rays, computed tomography (CT) and magnetic resonance imaging (MRI) scans: Results of a snapshot survey of English National Health Service (NHS) trusts,” 2015. [Online]. Available: https://www.rcr.ac.uk/sites/default/files/unreported_studies_feb2015.pdf.
- [3] P. Rajpurkar *et al.*, “CheXNet: Radiologist-Level Pneumonia Detection on Chest X-Rays with Deep Learning,” *arXiv Prepr. arXiv1711.05225*, 2017, [Online]. Available: <http://arxiv.org/abs/1711.05225>.
- [4] H. H. Pham, T. T. Le, D. Q. Tran, D. T. Ngo, and H. Q. Nguyen, “Interpreting chest X-rays via CNNs that exploit hierarchical disease dependencies and uncertainty labels,” *Neurocomputing*, vol. 437, pp. 186–194, 2021, doi: 10.1016/j.neucom.2020.03.127.
- [5] Z. Yuan, Y. Yan, M. Sonka, and T. Yang, “Large-scale Robust Deep AUC Maximization: A New Surrogate Loss and Empirical Studies on Medical Image Classification,” in *Proceedings of the IEEE/CVF International Conference on Computer Vision*, 2020, pp. 3040–3049, [Online]. Available: <http://arxiv.org/abs/2012.03173>.
- [6] J. Irvin *et al.*, “CheXpert: A large chest radiograph dataset with uncertainty labels and expert comparison,” in *33rd AAAI Conference on Artificial Intelligence, AAAI 2019, 31st Innovative Applications of Artificial Intelligence Conference, IAAI 2019 and the 9th AAAI Symposium on Educational Advances in Artificial Intelligence, EAAI 2019*, 2019, vol. 33, no. 01, pp. 590–597, doi: 10.1609/aaai.v33i01.3301590.
- [7] Morder Intelligence, “X-RAY FILM MARKET - GROWTH, TRENDS, COVID-19 IMPACT, AND FORECASTS (2021 - 2026),” 2020.
- [8] A. B. Schwartz *et al.*, “The accuracy of mobile teleradiology in the evaluation of chest X-rays,” *J. Telemed. Telecare*, vol. 20, no. 8, pp. 460–463, 2014, doi: 10.1177/1357633X14555639.
- [9] S. Andronikou *et al.*, “Paediatric radiology seen from Africa. Part I: Providing diagnostic imaging to a young population,” *Pediatr. Radiol.*, vol. 41, no. 7, pp. 811–825, 2011, doi: 10.1007/s00247-011-2081-8.
- [10] L. Liu *et al.*, “Application and preliminary outcomes of remote diagnosis and treatment during the COVID-19 outbreak: Retrospective cohort study,” *JMIR mHealth uHealth*,

vol. 8, no. 7, p. e19417, 2020, doi: 10.2196/19417.

- [11] K. Karako, P. Song, Y. Chen, and W. Tang, “Realizing 5G-and AI-based doctor-to-doctor remote diagnosis: opportunities, challenges, and prospects,” *Biosci. Trends*, 2020.
- [12] J. Liang, D. Doermann, and H. Li, “Camera-based analysis of text and documents: A survey,” *Int. J. Doc. Anal. Recognit.*, vol. 7, no. 2–3, pp. 84–104, 2005, doi: 10.1007/s10032-004-0138-z.
- [13] P. C. Kuo *et al.*, “Recalibration of deep learning models for abnormality detection in smartphone-captured chest radiograph,” *npj Digit. Med.*, vol. 4, no. 1, pp. 1–10, 2021, doi: 10.1038/s41746-021-00393-9.
- [14] C. F. Chong, X. Yang, W. Ke, and Y. Wang, “GAN-based Spatial Transformation Adversarial Method for Disease Classification on CXR Photographs by Smartphones,” in *2021 Digital Image Computing: Techniques and Applications (DICTA)*, 2021, pp. 01–08, doi: 10.1109/dicta52665.2021.9647192.
- [15] P. Rajpurkar, A. Joshi, A. Pareek, A. Y. Ng, and M. P. Lungren, “CheXternal: Generalization of deep learning models for chest X-ray interpretation to photos of chest X-rays and external clinical settings,” in *ACM CHIL 2021 - Proceedings of the 2021 ACM Conference on Health, Inference, and Learning*, 2021, pp. 125–132, doi: 10.1145/3450439.3451876.
- [16] A. Azulay and Y. Weiss, “Why do deep convolutional networks generalize so poorly to small image transformations?,” *arXiv Prepr. arXiv1805.12177*, 2018.
- [17] F. Zhan and S. Lu, “ESIR: End-to-end scene text recognition via iterative image rectification,” in *Proceedings of the IEEE Computer Society Conference on Computer Vision and Pattern Recognition*, 2019, vol. 2019-June, pp. 2054–2063, doi: 10.1109/CVPR.2019.00216.
- [18] I. Goodfellow *et al.*, “Generative adversarial nets,” *Adv. Neural Inf. Process. Syst.*, vol. 27, 2014.
- [19] K. Ma, Z. Shu, X. Bai, J. Wang, and D. Samaras, “DocUNet: Document Image Unwarping via a Stacked U-Net,” in *Proceedings of the IEEE Computer Society Conference on Computer Vision and Pattern Recognition*, 2018, pp. 4700–4709, doi: 10.1109/CVPR.2018.00494.

- [20] S. Das, K. Ma, Z. Shu, Di. Samaras, and R. Shilkrot, “DewarpNet: Single-image document unwarping with stacked 3D and 2D regression networks,” in *Proceedings of the IEEE International Conference on Computer Vision*, 2019, vol. 2019-Octob, pp. 131–140, doi: 10.1109/ICCV.2019.00022.
- [21] H. Feng, W. Zhou, J. Deng, Q. Tian, and H. Li, “DocScanner: Robust Document Image Rectification with Progressive Learning,” *arXiv Prepr. arXiv2110.14968*, 2021, [Online]. Available: <http://arxiv.org/abs/2110.14968>.
- [22] T. Björklund, A. Fiandrotti, M. Annarumma, G. Francini, and E. Magli, “Robust license plate recognition using neural networks trained on synthetic images,” *Pattern Recognit.*, vol. 93, pp. 134–146, Nov. 2019, doi: 10.1016/j.patcog.2019.04.007.
- [23] S. M. Silva and C. R. Jung, “A Flexible Approach for Automatic License Plate Recognition in Unconstrained Scenarios,” *IEEE Trans. Intell. Transp. Syst.*, 2021, doi: 10.1109/TITS.2021.3055946.
- [24] N. A. Phillips *et al.*, “CheXphoto: 10,000+ Photos and Transformations of Chest X-rays for Benchmarking Deep Learning Robustness,” in *Machine Learning for Health*, 2020, pp. 318–327, [Online]. Available: <http://arxiv.org/abs/2007.06199>.
- [25] “CheXphoto: A Perturbed Chest X-Ray Dataset and Competition.” <https://stanfordmlgroup.github.io/competitions/chexphoto/> (accessed Nov. 03, 2021).
- [26] H. X. Le, P. D. Nguyen, T. H. Nguyen, K. N. Q. Le, and T. T. Nguyen, “Interpretation of smartphone-captured radiographs utilizing a deep learning-based approach,” *arXiv Prepr. arXiv2009.05951*, 2020, [Online]. Available: <http://arxiv.org/abs/2009.05951>.
- [27] J. Redmon and A. Farhadi, “YOLOv3: An Incremental Improvement,” *arXiv Prepr. arXiv1804.02767*, 2018, [Online]. Available: <http://arxiv.org/abs/1804.02767>.
- [28] C. Solomon and T. Breckon, *Fundamentals of Digital Image Processing: A Practical Approach with Examples in Matlab*. John Wiley & Sons, 2011.
- [29] A. Creswell, T. White, V. Dumoulin, K. Arulkumaran, B. Sengupta, and A. A. Bharath, “Generative adversarial networks: An overview,” *IEEE Signal Process. Mag.*, vol. 35, no. 1, pp. 53–65, 2018.
- [30] K. Wang, C. Gou, Y. Duan, Y. Lin, X. Zheng, and F.-Y. Wang, “Generative adversarial networks: introduction and outlook,” *IEEE/CAA J. Autom. Sin.*, vol. 4, no. 4, pp. 588–

598, 2017.

- [31] Y. Fang, C. Deyun, and W. Rui, “A distortion correction approach on natural scene text image,” in *Proceedings of 2011 6th International Forum on Strategic Technology*, 2011, vol. 2, pp. 1058–1061.
- [32] J. Liang, D. DeMenthon, and D. Doermann, “Geometric rectification of camera-captured document images,” *IEEE Trans. Pattern Anal. Mach. Intell.*, vol. 30, no. 4, pp. 591–605, 2008.
- [33] Y. Takezawa, M. Hasegawa, and S. Tabbone, “Robust perspective rectification of camera-captured document images,” in *2017 14th IAPR International Conference on Document Analysis and Recognition (ICDAR)*, 2017, vol. 6, pp. 27–32.
- [34] Y.-H. Chang, C.-H. Chu, and M.-S. Chen, “A General Scheme for Extracting QR Code from a non-uniform background in Camera Phones and Applications,” in *Ninth IEEE International Symposium on Multimedia (ISM 2007)*, 2007, pp. 123–130.
- [35] H. Tribak and Y. Zaz, “QR code recognition based on principal components analysis method,” *Int. J. Adv. Comput. Sci. Appl*, vol. 8, pp. 241–248, 2017.
- [36] S. R. Deans, *The Radon transform and some of its applications*. Courier Corporation, 2007.
- [37] Y. Xiao and Z. Ming, “1D barcode detection via integrated deep-learning and geometric approach,” *Appl. Sci.*, vol. 9, no. 16, p. 3268, 2019.
- [38] A. Gupta, A. Vedaldi, and A. Zisserman, “Synthetic Data for Text Localisation in Natural Images,” in *Proceedings of the IEEE Computer Society Conference on Computer Vision and Pattern Recognition*, 2016, vol. 2016-Decem, pp. 2315–2324, doi: 10.1109/CVPR.2016.254.
- [39] D. Dwibedi, I. Misra, and M. Hebert, “Cut, Paste and Learn: Surprisingly Easy Synthesis for Instance Detection,” in *Proceedings of the IEEE International Conference on Computer Vision*, 2017, vol. 2017-Octob, pp. 1310–1319, doi: 10.1109/ICCV.2017.146.
- [40] F. Zhan, S. Lu, and C. Xue, “Verisimilar image synthesis for accurate detection and recognition of texts in scenes,” in *Lecture Notes in Computer Science (including subseries Lecture Notes in Artificial Intelligence and Lecture Notes in Bioinformatics)*, 2018, vol. 11212 LNCS, pp. 257–273, doi: 10.1007/978-3-030-01237-3_16.

- [41] C. H. Lin, E. Yumer, O. Wang, E. Shechtman, and S. Lucey, “ST-GAN: Spatial Transformer Generative Adversarial Networks for Image Compositing,” in *Proceedings of the IEEE Computer Society Conference on Computer Vision and Pattern Recognition*, 2018, pp. 9455–9464, doi: 10.1109/CVPR.2018.00985.
- [42] M. Jaderberg, K. Simonyan, A. Zisserman, and K. Kavukcuoglu, “Spatial transformer networks,” *Adv. Neural Inf. Process. Syst.*, vol. 2015-Janua, pp. 2017–2025, 2015.
- [43] K. He, X. Zhang, S. Ren, and J. Sun, “Deep residual learning for image recognition,” in *Proceedings of the IEEE Computer Society Conference on Computer Vision and Pattern Recognition*, 2016, vol. 2016-Decem, pp. 770–778, doi: 10.1109/CVPR.2016.90.
- [44] G. Huang, Z. Liu, L. Van Der Maaten, and K. Q. Weinberger, “Densely connected convolutional networks,” in *Proceedings - 30th IEEE Conference on Computer Vision and Pattern Recognition, CVPR 2017*, 2017, vol. 2017-Janua, pp. 2261–2269, doi: 10.1109/CVPR.2017.243.
- [45] R. I. Hartley, “Theory and practice of projective rectification,” *Int. J. Comput. Vis.*, vol. 35, no. 2, pp. 115–127, 1999, doi: 10.1023/A:1008115206617.
- [46] Jia Deng, Wei Dong, R. Socher, Li-Jia Li, Kai Li, and Li Fei-Fei, “ImageNet: A large-scale hierarchical image database,” in *2009 IEEE conference on computer vision and pattern recognition*, 2009, pp. 248–255, doi: 10.1109/cvprw.2009.5206848.
- [47] D. P. Kingma and J. L. Ba, “Adam: A method for stochastic optimization,” *3rd Int. Conf. Learn. Represent. ICLR 2015 - Conf. Track Proc.*, 2015.
- [48] T. Y. Lin *et al.*, “Microsoft COCO: Common objects in context,” in *Lecture Notes in Computer Science (including subseries Lecture Notes in Artificial Intelligence and Lecture Notes in Bioinformatics)*, 2014, vol. 8693 LNCS, no. PART 5, pp. 740–755, doi: 10.1007/978-3-319-10602-1_48.
- [49] Z. H. Zhou, *Ensemble methods: Foundations and algorithms*. Chapman and Hall/CRC, 2012.
- [50] L. K. Hansen and P. Salamon, “Neural Network Ensembles,” *IEEE Trans. Pattern Anal. Mach. Intell.*, vol. 12, no. 10, pp. 993–1001, 1990, doi: 10.1109/34.58871.
- [51] F. Chollet, “Xception: Deep learning with depthwise separable convolutions,” in *Proceedings - 30th IEEE Conference on Computer Vision and Pattern Recognition*,

CVPR 2017, 2017, vol. 2017-Janua, pp. 1800–1807, doi: 10.1109/CVPR.2017.195.